

1 **Revision 1**

2

3 **Mechanical properties of natural radiation damaged titanite and**  
4 **temperature induced structural reorganization: A Nanoindentation and**  
5 **Raman spectroscopic study**

6

7 Tobias Beirau<sup>1,2,\*</sup>, William D. Nix<sup>3</sup>, Rodney C. Ewing<sup>1</sup>, Gerold A. Schneider<sup>4</sup>, Lee A. Groat<sup>5</sup>,  
8 and Ulrich Bismayer<sup>2</sup>

9

10 <sup>1</sup>Department of Geological Sciences, Stanford University, Stanford, CA 94305-2115, U.S.A.

11 <sup>2</sup>Department of Earth Sciences, University of Hamburg, 20146 Hamburg, Germany

12 <sup>3</sup>Department of Materials Science and Engineering, Stanford University, Stanford, CA 94305-  
13 4034, U.S.A.

14 <sup>4</sup>Institute of Advanced Ceramics, Hamburg University of Technology, 21073 Hamburg,  
15 Germany

16 <sup>5</sup>Department of Earth, Ocean and Atmospheric Sciences, University of British Columbia,  
17 Vancouver, BC V6T 1Z4, Canada

18

19 \*Corresponding author, email: [tobiasbeirau@stanford.edu](mailto:tobiasbeirau@stanford.edu)

20

21 **Abstract**

22 This study provides new insights into the relation between thermally-induced  
23 structural reorganization and the macroscopic mechanical properties of radiation-damaged  
24 titanite. The natural sample contains ca. 30% amorphous fraction. Low temperature annealing  
25 affects only slightly the sample stiffness and leads to a softening resulting from the defect

26 annihilation in crystalline regions. In the high-temperature annealing regime, amorphous  
27 domains recrystallize and this leads to further recovery of defects, reduction of interfaces,  
28 grain growth, and, in general, an increase in the long-range order. The thermally-induced  
29 recrystallization is accompanied by massive dehydration leading to considerable stiffening  
30 and hardening. This interpretation of the recrystallization process in titanite based on the  
31 correlation of new results from nanoindentation and Raman-spectroscopic measurements  
32 complementing previous investigations using thermogravimetric and gas analyses by  
33 Hawthorne et al. (1991) and infrared spectroscopy by Zhang et al. (2001). The new data  
34 combined with previous work leads to a detailed description of the annealing behavior of a  
35 radiation-damaged titanite, which is a complicated process that includes dehydration and  
36 atomic-scale structural reorganization. In order to minimize the influence of surface  
37 phenomena on the hardness measurements, the so-called “true” hardness was used instead of  
38 the standard hardness calculation (Oliver and Pharr 1992). A comparison shows that the  
39 Oliver & Pharr method clearly underestimates the hardness.

40

41 **Keywords:** titanite, radiation damage,  $\alpha$ -decay, metamict, partially amorphous, dehydration,  
42 nanoindentation, Raman spectroscopy, true hardness, elastic modulus, recrystallization

43

44

## Introduction

45 Titanite is an accessory, nesosilicate mineral with end-member composition  $\text{CaTiSiO}_5$ .  
46 The ideal crystal structure consists of chains of corner-sharing,  $\text{TiO}_6$  octahedra, cross-linked  
47 by isolated  $\text{SiO}_4$  tetrahedra forming a  $\text{TiOSiO}_4$  framework which hosts  $\text{Ca}^{2+}$  -ions in irregular  
48  $\text{CaO}_7$  polyhedra (Speer and Gibbs 1976). Highly crystalline titanite close to its end-member  
49 composition undergoes a structural transition  $\text{P2}_1/\text{c} \leftrightarrow \text{C2}/\text{c}$  between monoclinic phases near  
50 500 K (Taylor and Brown 1976; Van Heurck et al. 1991; Bismayer et al. 1992; Salje et al.  
51 1993; Zhang et al. 1995; Meyer et al. 1996; Kek et al. 1997). Natural titanite incorporates

2

52 various impurities into its structure. Cations, like Al, Cr, Mn, Fe, Nb and Ta, can occupy the  
53 octahedrally coordinated Ti position (Paul et al. 1981; Hollabaugh and Foit Jr. 1984; Muir et  
54 al. 1984; Groat et al. 1985; Hawthorne et al. 1991; Chrosch et al. 1998; Gaft et al. 2003; Salje  
55 et al. 2011a). Tetrahedrally coordinated structural Si can be substituted by Ti, Cr and Fe  
56 (Hollabaugh and Rosenberg 1983; Gaft et al. 2003) and  $O^{2-}$  can be replaced by  $(OH)^-$  and  $F^-$   
57 (Hawthorne et al. 1991; Meyer et al. 1996;) as a result of charge compensation of cations or to  
58 fill vacancies. The seven-fold coordinated Ca in the titanite structure can be replaced by  
59 elements like Na, Mn, Y, Pb, REEs, Th and U (Hawthorne et al. 1991; Gaft et al. 2003).  
60 Further, actinides like U and Pu, neutron absorbing elements like Gd and Hf and also fission  
61 products like Sr have been incorporated into synthetic titanite (Ewing et al. 1995; Stefanovsky  
62 et al. 2000; Vance et al. 2000). Such impurities and radiation damage lead to domain wall  
63 pinning that hampers the phase transition in natural titanite (Meyer et al. 1996). Therefore its  
64 space group remains  $C2/c$  at room temperature on the XRD length scale. Nevertheless, Raman  
65 spectroscopy has revealed that the structural phase transition still occurs within the crystalline  
66 domains even in heavily damaged impure titanite (Beirau et al. 2014).

67 Mainly the  $\alpha$ -decay of incorporated radioactive elements leads to structural damage  
68 and amorphization in minerals (metamictization). This structural damage process has been  
69 described in great detail in the literature (i.e., Hawthorne et al. 1991; Ewing et al. 1995;  
70 Trachenko et al. 2001; Ewing 2007, 2011). The  $\alpha$ -decay of the unstable nucleus generates two  
71 different types of particles, an  $\alpha$ -particle, a  ${}^4_2He^{2+}$  core with an energy of  $\sim 4.5 - 5.8$  MeV (for  
72 actinides) and a heavy recoil nucleus with an energy of  $\sim 70 - 100$  keV. The smaller  $\alpha$ -  
73 particle displaces only several hundreds of atoms, mostly close to the end of its trajectory at  
74  $\sim 15 - 22$   $\mu m$ , inducing Frenkel defects in the structure by elastic collisions. The other particle  
75 is a heavier recoil nucleus displacing, in spite of lower kinetic energy ( $\sim 86$  keV for  ${}^{235}U$   
76 recoil from decay of  ${}^{239}Pu$ ), several thousands of atoms in its path of  $\sim 30 - 40$  nm through  
77 the crystal structure. In zircon ( $ZrSiO_4$ ) for example  $\sim 5000$  atoms are displaced per decay

78 event (Salje et al. 2012). The difference leading to displaced atoms is attributed to the fact that  
79 the  $\alpha$ -particle deposits most of its energy by ionization processes; whereas, the recoil nucleus  
80 loses its energy by elastic collisions. Therefore, the recoil nucleus introduces atomic recoil- or  
81 collision-cascades into the ordered structure. The overlap of these disordered aperiodic  
82 regions finally saturates and the long-range order is destroyed.

83 In titanite such radiation-induced structural changes can be described by the direct  
84 impact model (Weber 2000; Salje et al. 2012). Accordingly, recoil related discrete regions  
85 consisting of several thousand displaced atoms generate percolation paths by their overlap and  
86 create a composite structure of coexisting aperiodic and crystalline regions that are enriched  
87 in defects (Hawthorne et al. 1991; Lumpkin et al. 1991; Beirau et al. 2010, 2012; Salje et al.  
88 2011a, 2012). Between the radiation-induced amorphous regions and the crystalline matrix,  
89 interfaces with a less defined shape and an extremely heterogeneous internal structure emerge  
90 that modify the intrinsic elastic material properties of the mineral (Hawthorne et al. 1991).  
91 Because of the radiation damage, the strain in the titanite structure is increased and the unit  
92 cell volume expands ( $\sim 3\%$  in heavily damaged titanite) leading to an overall density decrease  
93 (Hawthorne et al. 1991). Spectroscopic techniques like X-ray absorption near-edge structure  
94 (XANES), extended X-ray absorption fine structure (EXAFS), infrared (IR), and Raman show  
95 that radiation-induced amorphization may also lead to a partial change of the Ti-coordination  
96 from six to five- and/or four-fold (Hawthorne et al. 1991; Farges 1997; Zhang et al. 2002;  
97 Beirau et al. 2012). Mössbauer spectroscopy confirms the persistence of short-range order  
98 even in the amorphous regions of the radiation-damaged titanite and shows that radiation-  
99 induced damage leads to a reduction of the oxidation state of initially incorporated  $\text{Fe}^{3+}$  to  
100  $\text{Fe}^{2+}$  (Hawthorne et al. 1991; Salje et al. 2011a).

101 From the thermodynamical point of view, the radiation-damaged structural state is  
102 metastable and can (at least partially) be recovered by thermal annealing that activates  
103 epitaxial recrystallization in damaged titanite (Vance and Metson 1985; Hawthorne et al.

104 1991; Paulmann et al. 2000; Zhang et al. 2002; Beirau et al. 2010, 2012). At low  
105 temperatures, annealing leads to recovery of defects in the crystalline domains; whereas, the  
106 recrystallization of the amorphous volume is initiated at temperatures above 600 K  
107 (Hawthorne et al. 1991; Paulmann et al. 2000; Beirau et al. 2010-2014; Zhang et al. 2013).

108 During or even after metamictization, major hydrogen contents are enriched in the  
109 aperiodic regions. This results in an increased number of OH-groups in damaged titanite  
110 leading to an expansion of the unit cell (Hawthorne et al. 1991; Zhang et al. 2001). IR  
111 spectroscopic measurements of radiation-damaged titanite show in the OH region additionally  
112 broad isotropic absorption features related to radiation-induced domains (Hawthorne et al.  
113 1991, Zhang et al. 2000, 2001; Salje et al. 2000). Using thermogravimetric and evolved gas  
114 analyses, Hawthorne et al. (1991) detected a loss of volatile species during high temperature  
115 annealing of titanite. IR spectroscopic analysis (Zhang et al. 2001) of radiation damaged and  
116 crystalline titanite also suggests that hydrogen is driven out during annealing.

117 This implies that hydrogen plays an important role during metamictization and  
118 recrystallization. The motivation of this work was to address the question of how the  
119 thermally-induced recrystallization affects the mechanical properties of titanite, particularly  
120 with regard to volatile species. Therefore, a well characterized titanite of an intermediate level  
121 of damage, a partially amorphous titanite sample (E2312), was chosen for this study. In the  
122 present work, we were able to develop a new model that correlates the thermally-induced  
123 changes of the macroscopic mechanical properties with atomic-scales rearrangements,  
124 accompanied by the loss of volatile hydrogen species. Previously published nanoindentation  
125 data from Beirau et al. (2013) have been reevaluated. We show that the method of Oliver and  
126 Pharr (Oliver and Pharr 1992) tends to underestimate the hardness as compared with new  
127 calculations of the so-called “true” hardness ( $H(E)$ ) (Saha and Nix 2002). The latter is less  
128 influenced by surface roughness and material behavior underneath the indenter tip, such as  
129 “pile-up” and “sink-in”. The true hardness and elastic modulus before and after annealing at

130 different temperature steps correlate well with the results of Raman spectroscopic  
131 measurements, which were performed after each indentation cycle and provide insights into  
132 the structural behavior on the local length scale. This new model combines the new results  
133 with previously published data obtained by thermogravimetric and evolved gas analyses, X-  
134 ray diffraction, Raman and infrared spectroscopic measurements of the E2312 titanite (see  
135 Hawthorne et al. 1991; Zhang and Salje 2003; Zhang et al. 2001, 2002, 2013; Beirau et al.  
136 2013).

137

## 138 **Experimental methods**

139

### 140 **Partially amorphous titanite E2312**

141 A partially amorphous titanite sample from Sebastopol Township in Ontario, Canada,  
142 was selected because its intermediate level of radiation damage should contain both  
143 amorphous and defect-rich crystalline domains. This sample was obtained from the Royal  
144 Ontario Museum in Toronto, catalog number E2312. This radiation-damaged titanite has been  
145 extensively characterized by various methods, e.g., electron microprobe, thermogravimetric  
146 and evolved gas analyses, X-ray diffraction and nuclear magnetic resonance (NMR), mass,  
147 Mössbauer, IR, and Raman spectroscopy (Hawthorne et al. 1991; Zhang and Salje 2003;  
148 Zhang et al. 2001, 2002, 2013; Salje et al. 2011a, 2012). E2312 contains ca. 30 % amorphous  
149 fraction and an amount of U and Th of  $\sim 170 - 204$  and  $716 - 860$  ppm, respectively (Salje et  
150 al. 2012). The amount of F and  $\text{Fe}_2\text{O}_3$  is 1.64 and 2.89 wt%, respectively (Hawthorne et al.  
151 1991). This titanite is  $\sim 1.053 \times 10^9$  years old, giving an  $\alpha$ -decay dose of  $1.26 - 1.49 \times 10^{18}$   $\alpha$ -  
152 events  $\text{g}^{-1}$  (Salje et al. 2012). The dimensions of E2312 were  $\sim 2 \times 1 \times 0.5 \text{ mm}^3$  with unit cell  
153 parameters of  $\mathbf{a} = 6.562(1) \text{ \AA}$ ,  $\mathbf{b} = 8.715(2) \text{ \AA}$ ,  $\mathbf{c} = 7.076(1) \text{ \AA}$ , and  $\beta = 113.94(2)^\circ$  leading to a  
154 unit cell volume of  $369.8(1) \text{ \AA}^3$  (Hawthorne et al. 1991).

155

156 **Annealing**

157 Titanite E2312 was annealed in air in steps at 600, 950 and 1220 K for two hours at  
158 each step using a Thermo Scientific Laboratory Chamber Furnace K114. The temperature was  
159 controlled by an AHLBORN THERM 2420 device equipped with a NiCr–Ni thermocouple,  
160 ensuring thermal stability of  $\pm 2$  K. The heating period between steps was always  $\sim 35$  min.  
161 After each annealing step, the titanite was cooled down to room temperature and  
162 nanoindentation and Raman measurements were performed.

163

164 **Nanoindentation**

165 The mechanical properties of the titanite sample were measured using an Agilent Nano  
166 Indenter G200 equipped with a Berkovich indenter tip (diamond XP indentation head),  
167 operated in the continuous stiffness mode (CSM). The indentations were made using a  
168 constant nominal strain rate of  $0.05 \text{ s}^{-1}$ . Using CSM the sample stiffness ( $S$ ) is measured  
169 continuously in the course of the loading process of the indenter (see Li and Bhushan 2002;  
170 Oliver and Pharr 2004). A small dynamic oscillation is imposed on the force or displacement  
171 signal, and the amplitude and phase of the corresponding signal is measured with a frequency-  
172 specific amplifier. The measurements were performed on a polished plane-parallel specimen.  
173 Six to seven indents were made in the virgin sample and after each annealing step. The  
174 indentations were distributed over the entire sample surface ( $22\bar{3}$ ) in order to ensure  
175 significant average results. The instrument software calculated the hardness ( $H$ ) (referred in  
176 this paper as  $H(O\&P)$  after Saha and Nix (2002)) and the elastic modulus ( $E$ ) during the  
177 loading process using the method of Oliver & Pharr (1992) developed for monolithic  
178 materials.  $H(O\&P)$  is defined by

179 
$$H = \frac{P}{A} \quad (1)$$

180 where  $P$  is the imposed load and  $A$  the projected contact area between the indenter and the  
181 sample determined from the shape of the indenter and using the Oliver and Pharr method  
182 (Joslin and Oliver 1990; Oliver and Pharr 2004).

183 The measured contact stiffness ( $S$ ) is related to the elastic properties of both, the  
184 sample and indenter; and the contact area through (Sneddon 1965)

$$185 \quad S = \beta \frac{2}{\sqrt{\pi}} E_r \sqrt{A} \quad (2)$$

186 where  $\beta$  is a constant depending on the indenter geometry (for Berkovich geometry  $\beta = 1.034$ )  
187 (Pharr 1998) and  $E_r$  is the reduced modulus given by

$$188 \quad \frac{1}{E_r} = \frac{(1-\nu_i^2)}{E_i} + \frac{(1-\nu^2)}{E} \quad (3)$$

189 where  $E_i$  and  $\nu_i$  are elastic modulus and Poisson's ratio of the indenter, respectively (for the  
190 diamond indenter  $E_i = 1141$  GPa and  $\nu_i = 0.07$ ) and  $E$  and  $\nu$  are the elastic properties of the  
191 sample (Oliver and Pharr 2004).  $E_r$  considers that elastic displacement takes place in the  
192 sample and in the indenter (Oliver and Pharr 2004).

193 Equations (1), (2) and (3) show that both the hardness and modulus require knowledge  
194 of the contact area ( $A$ ). While the Oliver and Pharr method is available for determining  $A$  from  
195 the known shape of the indenter, measured loads, and displacements in the case of smooth  
196 surfaces (Oliver and Pharr 2004), that method leads to errors for rough surfaces or when pile-  
197 up or sink-in occurs (Saha and Nix 2002). In these cases, it is better to eliminate the contact  
198 area by combining equations (1) and (2) to read (Joslin and Oliver 1990)

$$199 \quad H(E) = \frac{4}{\pi} \beta^2 E_r^2 \left( \frac{P}{S^2} \right) \quad (4)$$

200 where  $H(E)$  is now the so-called true hardness or true contact pressure that can be determined  
201 from the measured load ( $P$ ) and stiffness ( $S$ ), provided that the elastic modulus is known,  
202 without any knowledge of the contact area ( $A$ ) (Saha and Nix 2002).

203



## 204 **Raman spectroscopy**

205 Raman spectra were recorded from the same sample and the same crystallographic  
206 plane (22 $\bar{3}$ ). The measurements were performed on a polished plane-parallel specimen using  
207 a Horiba Jobin-Yvon T64000 triple monochromator system operating in a subtractive regime  
208 and equipped with a liquid N<sub>2</sub>-cooled charge-coupled device (CCD) detector and an Olympus  
209 BH41 microscope. Spectra were collected in back-scattering geometry without analyzer of the  
210 scattered light, using the 514.5 nm line of an Ar<sup>+</sup>-ion laser and a long-working distance  
211 objective with magnification 50 $\times$ . The Raman spectroscopic system was always calibrated to  
212 the position of the Si peak at 520.5 cm<sup>-1</sup> with a precision of  $\pm 0.35$  cm<sup>-1</sup>. The measured spectra  
213 were reduced by the Bose-Einstein occupation factor  $\{I_{reduced} = I_{measured}/[n(\omega, T) + 1], n(\omega, T) =$   
214  $1/(e^{\hbar\omega/kT} - 1)\}$  and fitted by Lorentzian functions using the software package Origin 8.5, to  
215 determine the peak positions, full-widths at half maximum (FWHM), and integrated  
216 intensities.

217

## 218 **Results and discussion**

219

### 220 **Determination of Nanoindentation Hardness: True hardness calculation vs Oliver &** 221 **Pharr method**

222 The hardness determination after Oliver and Pharr (1992) has become a standard method in  
223 evaluating nanoindentation data. It uses the contact area between the indenter tip and the  
224 sample for determination of  $H$  as followed from equation (1). In order to obtain results for  $H$   
225 which are less influenced by indentation-related surface phenomena, surface roughness or  
226 misalignment, we calculated the true hardness (eq. 4) for comparison. Hence, the mechanical  
227 property,  $\frac{P}{S^2}$ , provides an indication of the material's resistance to plastic deformation (Joslin  
228 and Oliver 1990) (Fig. 1; Table 1). This parameter is fully independent of the contact area, as

229 it is calculated from the directly measured  $P$  and  $S$  data. Its behavior is related to annealing  
230 and will be analyzed in the next section. According to equation (4) for the true hardness  
231 calculation, the reduced modulus is also needed. It was determined by equation (3) using the  
232 average elastic modulus received from the CSM measurements and a  $\nu$ -value of 0.18. The  
233 Poisson's ratio was estimated based on its similarity to other hard and brittle ceramics or  
234 minerals, which typically have values like this (e.g., Greaves et al. 2011). We calculated the  
235 average elastic modulus of the sample after each annealing step at an indentation depth of 700  
236  $\pm$  21 nm to ascertain correct values that were not influenced by roughness uncertainties at low  
237 indentation depths or cracking at higher depths (Fig. 2; Table 1). It is important to use a  
238 constant  $E_r$  for  $\frac{P}{S^2}$  calculations in order to assure that the calculated true hardness evolution  
239 with increasing indentation depth is influenced only by variations in  $P$  and  $S$ .

240         The evolution of  $H(E)$  and  $H(O\&P)$  with increasing indentation depth is shown on the  
241 basis of selected representative indents after annealing at different temperatures in Figure 3.  
242 The corresponding load displacement curves are displayed in Figure 4. As can be seen after  
243 annealing at 950 and 1220 K, the sample becomes brittle, which is indicated by an increasing  
244 number of pop-ins. Accordingly, we decided to determine the sample harnesses ( $H(E)$  and  
245  $H(O\&P)$ ) at an indentation depth of 600  $\pm$  21 nm where the indentation hardness was already  
246 stabilized and the influence of cracking is minimized (Fig. 5; Table 1). The results reveal that  
247 the Oliver & Pharr method underestimates the hardness of the sample in average by  $\sim$  0.8 GPa  
248 which cannot be neglected concerning a maximum annealing-induced change of  $H(E)$  of  $\sim$  2.3  
249 GPa (Fig. 3,5; Table 1). However, the trend of  $H$  calculated after both methods remains the  
250 same. The annealing induced changes are described in detail in the next section.

251

## 252 **Annealing-induced structural reorganization**

253 **I. Low temperature annealing – Healing of defects in crystalline areas.** The first  
254 annealing for two hours was done at 600 K. After this step, titanite E2312 shows a decrease of  
255 the true hardness from 12.4 GPa to 11.7 GPa and also of the elastic modulus from 161.2 GPa  
256 to 157.4 GPa (Fig. 2; Table 1). The nanoindentation load-displacement (LD) data obtained at  
257 RT from the virgin titanite sample and after annealing at 600 K show nearly no cracking with  
258 increasing indentation depth (Figs. 4a,b). The material parameter  $\frac{P}{s^2}$  shows a slight decrease  
259 from 430.2 to 422.9 nm<sup>2</sup>/mN (Fig. 1; Table 1), which indicates that the resistance to plastic  
260 deformation shows no significant change up to this annealing step. Also the Raman modes  
261 near 233 cm<sup>-1</sup> and 423 cm<sup>-1</sup> (the latter is related to O-Si-O bending) reveal almost no  
262 modifications in this temperature regime, indicating no significant structural changes on the  
263 local length scale after low temperature annealing (Figs. 6,7,8; Table 2). The results are in  
264 good agreement with previous Raman spectroscopic measurements, presenting the same  
265 selected modes of titanite E2312 annealed in N<sub>2</sub> atmosphere by Zhang et al. (2013) and  
266 synchrotron XRD measurements (Beirau et al. 2013). Thermogravimetric and evolved gas  
267 analyses performed on E2312 titanite also indicate no detectable volatiles escaping from the  
268 structure (Hawthorne et al. 1991). These observations are consistent with the assumption that  
269 annealing of titanite up to ~ 650 K only leads to the healing of defects in the crystalline parts  
270 of the mineral (Bismayer et al. 2010, Beirau et al. 2010-2014). This defect annihilation  
271 enables increasing dislocation mobility in the crystalline areas resulting in lower sample  
272 hardness. Hence, it can be inferred that the slight decrease in elastic modulus is related to the  
273 recovery of defects and the loss of interstitials. The theoretical approach of Dienes (1952)  
274 indicates that in simple cubic metals, interstitials increase the mass density, which leads to a  
275 slight increase in *E*, exceeding the non-linear weakening effect of vacancies (Dienes 1952,  
276 1953; Ledbetter and Reed 1973; Lizhi and Zhu 2004).  
277

278 **II. High-temperature annealing – Recrystallization of amorphous areas.** Two  
279 hours annealing at 950 K leads to a further decrease of  $H(E)$  to 10.1 GPa, while  $E$  increases  
280 up to 163.2 GPa (Fig. 2; Table 1). The LD curves show that the sample has become brittle  
281 after this annealing step, as indicated by several cracks and corresponding to steps in the slope  
282 (Fig. 4c). The ongoing and even stronger decrease in  $H(E)$  is attributed to extensive structural  
283 rearrangements. This is supported by the results of Raman spectroscopic measurements  
284 obtained from the same titanite sample E2312 after annealing at 950 K and indentation (Figs.  
285 6,7,8). The modes near  $233\text{ cm}^{-1}$  and  $423\text{ cm}^{-1}$  show an increase in band position up to  $\sim 237$   
286  $\text{cm}^{-1}$  and  $\sim 427\text{ cm}^{-1}$ , respectively and a decrease in full-width at half-maximum (FWHM)  
287 from  $\sim 22\text{ cm}^{-1}$  to  $\sim 12\text{ cm}^{-1}$  and  $\sim 37\text{ cm}^{-1}$  to  $\sim 32\text{ cm}^{-1}$ , respectively, which displays an  
288 increased order on the local length scale (Figs. 6,7,8., Table 2). Results of earlier Raman  
289 studies of E2312 titanite by Zhang et al. (2013) are similar to ours and show large changes in  
290 the evolution of the Raman bands at 700 – 800 K, which are attributed to thermal  
291 recrystallization of the amorphous areas in the radiation-damaged sample. Previously reported  
292 synchrotron XRD measurements on E2312 also prove the reestablishment of the long-range  
293 order after this annealing step (Beirau et al. 2013). Therefore, the structural reorganization  
294 accompanied by grain growth effects and defect annihilation leads to further softening,  
295 because grain growth reduces the number of grain boundaries that impede dislocation motion  
296 and contribute to sample hardness. Hence, in this annealing region titanite shows a classical  
297 Hall-Petch behavior (Hall 1951; Petch 1953), which includes a recrystallization-related  
298 reduction of the resistance to plastic deformation of titanite E2312, as indicated by a  
299 noticeable drop of  $\frac{P}{S^2}$  from 422.9 to 342.5  $\text{nm}^2/\text{mN}$  (Fig. 1; Table 1). The observed sample  
300 stiffening indicated by increased  $E$  supports the assumptions and is consistent with increasing  
301 sample crystallinity (Fig. 2). Increasing bond-strength and the formation of new bonds due to  
302 recrystallization of the amorphous regions stiffens the material. The annealing step at 950 K

303 does not necessarily show the minimum of  $H(E)$ , but perhaps already is in a re-hardened  
304 stage, which is in agreement with the vibrational data (Figs. 6,7,8). Unfortunately, records of  
305 further intermediate annealing steps were not possible, because of the increasing sample  
306 brittleness related to thermal annealing.

307 Thermal annealing at 1220 K increases the true hardness, as well as the elastic  
308 modulus (Fig. 2; Table 1).  $H(E)$  reaches 11.2 GPa and  $E$  171.3 GPa. The material remains  
309 very brittle as indicated by fracturing during indentation (Fig. 4d). The material parameter  $\frac{P}{S^2}$   
310 displays no relevant changes, only a very slight increase to 348.8 nm<sup>2</sup>/mN (Fig. 1; Table 1).  
311 The Raman band positions show almost saturation as well as the FWHMs, which slightly  
312 decrease to  $\sim 10$  and  $\sim 28$  cm<sup>-1</sup>, respectively (Figs. 6,7,8, Table 2). Combined with the Raman  
313 data from Zhang et al. (2013) and synchrotron data (Beirau et al. 2013) of E2312 titanite, the  
314 major structural reorganization is almost completed by 1100 K. Based on infrared  
315 spectroscopic analyses of anisotropic and isotropic OH signals in titanite, with different  
316 degrees of structural damage, Zhang et al. (2001) could show the enrichment of OH in  
317 amorphous regions resulting from radiation damage. They reported in virgin E2312 titanite an  
318 OH concentration of 0.59 wt% H<sub>2</sub>O in the amorphous and 0.02 wt% H<sub>2</sub>O in the crystalline  
319 fraction. The presence of hydrogen in the sample probably affects the overall bonding in the  
320 material, making it also more compliant and softer. Annealing-induced recrystallization leads  
321 to dehydration of these areas (Hawthorne et al. 1991; Salje et al. 2000; Zhang et al. 2001).  
322 The OH species seem to be another type of defect in titanite (Zhang et al. 2001) annihilated  
323 during annealing at higher temperatures. Thermogravimetric and evolved gas analyses  
324 performed by Hawthorne et al. (1991) report a weight loss of 0.06 wt% in titanite E2312 in  
325 the temperature range of 873 – 1273 K with H<sub>2</sub> as the principal volatile species and only  
326 minor H<sub>2</sub>O. We attribute the observed remarkable hardening and stiffening between the  
327 annealing steps of 950 and 1220 K to the temperature-induced structural loss of hydrogen

328 during the course of recrystallization. This is supported by infrared spectroscopic  
329 measurements of another heavily-radiation damaged titanite from Cardiff (M28696) showing  
330 that almost all the OH disappears from the amorphous regions during annealing between ~  
331 700 and 1000 K (Zhang et al. 2001). Their observations indicate considerable hydrogen  
332 diffusion at annealing temperatures of 800 - 900 K from damaged to crystalline regions,  
333 where it is incorporated into the crystal structure. Dehydration of the crystalline parts in  
334 heavily damaged Cardiff titanite and in crystalline titanite (No. 12) was reported near 1000  
335 and 1100 K respectively (Zhang et al. 2001). Both radiation damaged titanites (M28696 and  
336 E2312) show a remarkable loss of H<sub>2</sub> at 773 K < T < 1273 K (Hawthorne et al. 1991) and  
337 dehydration seems to be the dominating effect between 950 and 1220 K superimposed on the  
338 expected softening related to grain growth, defect annihilation and reduction of interface  
339 areas. One might think of hydrogen as “lubricating” the partially amorphous titanite, making  
340 it on average more compliant and softer. As seen from the *H(E)* and *E* values of the virgin  
341 sample, this effect is obscured by radiation-hardening at lower annealing temperatures.

342

343

### Implications

344

345 A better understanding of radiation-induced structural damage and thermally-induced  
346 recrystallization on the macroscopic mechanical properties of condensed matter is of great  
347 importance in the search and development of suitable host matrices for the long-term disposal  
348 of nuclear waste, particularly actinides, which decay mainly by  $\alpha$ -decay events. In this  
349 context, this study on radiation-damaged titanite shows how complex the interactions are  
350 between radiation-induced amorphization on the local length scale and macroscopic material  
351 behavior. Natural titanite is an ideal model substance for the study of radiation damage  
352 phenomena, because it accumulates  $\alpha$ -decay induced structural damage, often over hundreds  
353 of millions of years. Also in mid-1980's, titanite was proposed as a possible host matrix for

14

354 nuclear waste, particularly for fission-product elements, such as Sr, by the Atomic Energy of  
355 Canada Limited (Dixton 1986; Hayward 1988; Ewing et al. 1995). Previously performed  
356 resonant ultrasound spectroscopic (RUS) measurements of a different, less damaged titanite  
357 (E2335) show a temperature shift and more extreme behavior of the softest shear moduli as  
358 compared with our results of  $E$  (Salje et al. 2011b). This is probably caused by the different  
359 sample properties (variations in chemistry and different degrees of structural damage) and /or  
360 the method of analysis. In contrast to studies on other radiation damaged materials, e.g., Cm-  
361 doped  $Gd_2Ti_2O_7$  and  $CaZrTi_2O_7$ , and zircon (Weber et al. 1986, 1998; Chakoumakos et al.  
362 1991; Oliver et al. 1994) where the hardness is reported to decrease with increasing  $\alpha$ -decay  
363 dose, titanite E2312 shows an unusual hardness behavior. Hardness measurements after  
364 stepwise annealing of  $AB_2O_6$  type Ti-Nb-Ta oxides also show an increasing hardness with  
365 increasing temperature (Ewing 1973). Weber et al. (1986) have noted that the observed  
366 radiation dose-related decrease in hardness is not yet fully understood. A recrystallization  
367 pattern in which the hardness first decreases and then increases as in the case of titanite, may  
368 have further analogues in radiation-damaged minerals. Therefore, it will be very interesting to  
369 investigate in the future the hardness behavior in general and especially the influence of OH  
370 groups or  $H_2O$  in more detail in radiation-damaged materials, including minerals containing  
371 them as original structural constituents. The results of this investigation imply that using the  
372 true hardness instead of the hardness calculated after the Oliver and Pharr method is not only  
373 suitable in investigations of thin films (Saha and Nix 2002), but may also be extended to  
374 investigations of minerals.

375

### 376 **Acknowledgements**

377 The work leading to this publication was supported by the German Academic  
378 Exchange Service (DAAD) with funds from the German Federal Ministry of Education and  
379 Research (BMBF) and the People Programme (Marie Curie Actions) of the European Union's

380 Seventh Framework Programme (FP7/2007-2013) under REA grant agreement n° 605728  
381 (P.R.I.M.E. - Postdoctoral Researchers International Mobility Experience). Financial support  
382 by the DFG via SPP 1415 and the University of Hamburg is gratefully acknowledged. We  
383 wish to thank Paula Guglielmi and Borianna Mihailova for support during the measurements.  
384 The constructive comments and helpful suggestions of two anonymous reviewers are  
385 gratefully acknowledged.

386

387

### References cited

388

389 Beirau, T., Bismayer, U., Mihailova, B., Paulmann, C., and Groat, L. (2010) Structural  
390 phenomena of metamict titanite: a synchrotron, X-ray diffraction and vibrational  
391 spectroscopic study. *Phase Transitions*, 83, 694–702.

392

393 Beirau, T., Mihailova, B., Matveeva, G., Kolb, U., Malcherek, T., Groat, L.A., and Bismayer,  
394 U. (2012) Structural anisotropy and annealing-induced nanoscale atomic  
395 rearrangements in metamict titanite. *American Mineralogist*, 97, 1354-1365.

396

397 Beirau, T., Guglielmi, P., Paulmann, C., Schneider, G. A., Groat, L. A., Malcherek, T., Salje,  
398 E.K.H., and Bismayer, U. (2013) Interfaces in metamict titanite: the macroscopic  
399 mechanical properties after stepwise annealing. *Phase Transitions*, 86, 23-32.

400

401 Beirau, T., Mihailova, B., Malcherek, T., Paulmann, C., Groat, L. A., and Bismayer, U.  
402 (2014) Temperature-induced  $P2_1/c$  to  $C2/c$  phase transition in partially amorphous  
403 (metamict) titanite revealed by Raman spectroscopy. *Canadian Mineralogist*, 52, 91-  
404 100.

405



- 406 Bismayer, U., Schmahl, W., Schmidt, C., and Groat, L.A. (1992) Linear Birefringence and X-  
407 Ray Diffraction Studies of the Structural Phase Transition in Titanite, CaTiSiO<sub>5</sub>.  
408 Physics and Chemistry of Minerals, 19, 260–266.  
409
- 410 Bismayer, U., Paulmann, C., Groat, L.A., and Zhang, M. (2010) Local Phenomena in  
411 metamict Titanite. Acta Physica Polonica A 117, 74–77.  
412
- 413 Chakoumakos, B.C., Oliver, W.C., Lumpkin, G.R., and Ewing, R.C. (1991) Hardness and  
414 elastic modulus of zircon as a function of heavy-particle irradiation dose: I. In situ  $\alpha$ -  
415 decay event damage. Radiation Effects and Defects in Solids, 118, 393-403  
416
- 417 Chrosch, J., Colombo, M., Malcherek, T., Salje, E.K.H., Groat, L.A., and Bismayer, U. (1998)  
418 Thermal annealing of radiation damaged titanite. American Mineralogist, 83, 1083–  
419 1091.  
420
- 421 Dienes, G.J. (1952) A theoretical estimate of the effect of radiation on the elastic constants of  
422 simple metals. Physical Review, 86, 228-234.  
423
- 424 Dienes, G.J. (1953) Effects of nuclear radiation on the mechanical properties of solids\*.  
425 Journal of Applied Physics, 24, 666-674.  
426
- 427 Dixton, R.S. (1986) The Canadian Nuclear Fuel Waste Management Programm a summary of  
428 the Program and Progress to 1984 December. Scientific Document Distribution Office  
429 Atomic Energy of Canada Limited, Chalk River, Ontario, Canada. ISSN 0067–0367.  
430

- 431 Ewing, R.C. (1973) Vickers Hardness and Reflectance Determinations for Metamict AB<sub>2</sub>O<sub>6</sub>-  
432 Type Rare Earth Ti-Nb-Ta Oxides. American Mineralogist, Volume 58, pages 942-  
433 944.
- 434
- 435 Ewing, R.C. (2007) Displaced by radiation. Nature, 445, 161-162.
- 436
- 437 Ewing, R.C. (2011) Actinides and radiation effects: impact on the back-end of the nuclear fuel  
438 cycle. Mineralogical Magazine, 75, 2359-2377.
- 439
- 440 Ewing, R.C., Weber, W.J., and Clinard Jr., F.W. (1995) Radiation effects in nuclear waste  
441 forms for high-level radioactive waste. Progress in Nuclear Energy, 29, 63-127.
- 442
- 443 Farges, F. (1997) Fivefold-coordinated Ti<sup>4+</sup> in metamict zirconolite and titanite: A new  
444 occurrence shown by Ti K-edge XANES spectroscopy. American Mineralogist, 82,  
445 44–50.
- 446
- 447 Gaft, M., Nagli, L., Reisfeld, R., and Panczer, G. (2003) Laser-induced time-resolved  
448 luminescence of natural titanite CaTiOSiO<sub>4</sub>. Optical Materials, 24, 231-241.
- 449
- 450 Greaves, G.N., Greer, A.L., Lakes, R.S., and Rouxel, T. (2011) Poisson's ratio and modern  
451 materials. Nature Materials, 10, 823-837.
- 452
- 453 Groat, L.A., Carter, R.T., Hawthorne, F.C., and Ercit, T.S. (1985) Tantalian niobian titanite  
454 from the Irgon Claim, Southeastern Manitoba. Canadian Mineralogist, 23, 569-571.
- 455

- 456 Hall, E.O. (1951) The Deformation and Ageing of Mild Steel: III Discussion of Results.  
457 Proceedings of the Physical Society of London Section B, 64, 747-753.  
458
- 459 Hawthorne, F.C., Groat, L.A., Raudsepp, M., Ball, N.A., Kimata, M., Spike, F., Gaba, R.,  
460 Halden, N.M., Lumpkin, G.R., Ewing, R.C., and others. (1991) Alpha-decay damage  
461 in titanite. American Mineralogist, 76, 370–396.  
462
- 463 Hayward, P.J. (1988) Glass-ceramics. In W. Lutze and R.C. Ewing. Eds., Radioactive Waste  
464 Forms for the Future, p. 427-494. North-Holland Physics Publishing, Netherlands.  
465
- 466 Hollabaugh, C.L., and Foit, F.F. Jr. (1984) The crystal structure of an Al-rich titanite from  
467 Grisons, Switzerland. American Mineralogist, 69, 725-732.  
468
- 469 Hollabaugh, C.L., and Rosenberg, P.E. (1983) Substitution of Ti for Si in titanite and new  
470 end-member cell dimensions for titanite. American Mineralogist, 68, 177-180.  
471
- 472 Joslin D.L., and Oliver, W.C. (1990) A new method for analyzing data from continuous  
473 depth-sensing microindentation tests. Journal of Materials Research, 5, 123-126.  
474
- 475 Kek, S., Aroyo, M., Bismayer, U., Schmidt, C., Eichhorn, K., and Krane, H.G. (1997) The  
476 two-step phase transition of titanite, CaTiSiO<sub>5</sub>: a synchrotron radiation study.  
477 Zeitschrift für Kristallographie, 212, 9–19.  
478
- 479 Ledbetter, H.M., and Reed, R.P. (1973) Elastic Properties of Metals and Alloys, 1. Iron,  
480 Nickel, and Iron-Nickel Alloys. Journal of Physical and Chemical Reference Data, 2,  
481 531-617.

482

483 Li, X., and Bhushan, B. (2002) A review of nanoindentation continuous stiffness  
484 measurement technique and its applications. *Materials Characterization*, 48, 11-36.

485

486 Lizhi, O., and Zhu, D.M. (2004) Simulation of the Effect of Interstitials to Shear Modulus in  
487 Aluminum and Ionic Crystal. In M. Tokuyama and I. Oppenheim, Eds., *Proceedings*  
488 *of the 3rd International Symposium on Slow Dynamics in Complex Systems*, p. 715-  
489 716. AIP Conference Proceedings, Sendai.

490

491 Lumpkin, G.R., Eby, R.K., and Ewing, R.C. (1991) Alpha-recoil damage in titanite  
492 (CaTiSiO<sub>5</sub>): Direct observation and annealing study using high resolution  
493 transmission electron microscopy. *Journal of Materials Research*, 6, 560–564.

494

495 Meyer, H.W., Zhang, M., Bismayer, U., Salje, E.K.H., Schmidt, C., Kek, S., Morgenroth, W.,  
496 and Bleser, T (1996) Phase transformation of natural titanite: An infrared, Raman  
497 spectroscopic, optical birefringence and X-ray diffraction study. *Phase Transitions*, 59,  
498 39-60.

499

500 Muir, I.J., Metson, J.B., and Bancroft, G.M. (1984) <sup>57</sup>Fe Mössbauer spectra of perovskite and  
501 titanite. *Canadian Mineralogist*, 22, 689-694.

502

503 Oliver, W.C., and Pharr, G.M. (1992) An improved technique for determining hardness and  
504 elastic modulus using load and displacement sensing indentation experiments. *Journal*  
505 *of Materials Research*, 7, 1564–1583.

506

- 507 Oliver, W.C., and Pharr, G.M. (2004) Measurement of hardness and elastic modulus by  
508 instrumented indentation: Advances in understanding and refinements to  
509 methodology. *Journal of Materials Research*, 19, 3–20.
- 510
- 511 Oliver, W.C., McCallum, J.C., Chakoumakos, B.C., and Boatner, L.A. (1994) Hardness and  
512 elastic modulus of zircon as a function of heavy-particle irradiation dose: II. Pb-ion  
513 implantation damage\*. *Radiation Effects and Defects in Solids*, 132, 131-141.
- 514
- 515 Paul, B.J., Cerny, P., and Chapman, R. (1981) Niobian titanite from the huron claim  
516 pegmatite, southeastern Manitoba. *Canadian Mineralogist*, 19, 549-552.
- 517
- 518 Paulmann, C., Bismayer, U., and Groat, L.A. (2000) Thermal annealing of metamict titanite:  
519 A synchrotron radiation and optical birefringence study. *Zeitschrift für*  
520 *Kristallographie*, 215, 678–682.
- 521
- 522 Petch, N.J. (1953) The cleavage strength of polycrystals. *Journal of the Iron and Steel*  
523 *Institute*, 174, 25-28.
- 524
- 525 Pharr, G.M. (1998) Measurement of mechanical properties by ultra-low load indentation.  
526 *Materials Science and Engineering: A*, 253, 151–159.
- 527
- 528 Saha, R., and Nix, W.D. (2002) Effects of the substrate on the determination of thin film  
529 mechanical properties by Nanoindentation. *Acta Materialia*, 50, 23–38
- 530

- 531 Salje, E.K.H., Schmidt, C., and Bismayer, U. (1993) Structural Phase Transition in Titanite,  
532 CaTiSiO<sub>5</sub>: A Raman spectroscopic Study. *Physics and Chemistry of Minerals*, 19,  
533 502–506.
- 534
- 535 Salje, E.K.H., Zhang, M., and Groat, L.A. (2000) Dehydration and recrystallization of  
536 radiation-damaged titanite under thermal annealing. *Phase Transitions*, 71, 173-187.
- 537
- 538 Salje, E.K.H., Safarik, D.J., Taylor, R.D., Pasternak, M.P., Modic, K.A., Groat, L.A., and  
539 Lashley, J.C. (2011a) Determination of iron sites and the amount of amorphization in  
540 radiation-damaged titanite (CaSiTiO<sub>5</sub>). *Journal of Physics: Condensed Matter*, 23,  
541 105402 (3 p).
- 542
- 543 Salje, E.K.H., Safarik, D.J., Lashley, J.C., Groat, L.A., and Bismayer, U. (2011b) Elastic  
544 softening of metamict titanite CaTiSiO<sub>5</sub>: Radiation damage and annealing. *American*  
545 *Mineralogist*, 96, 1254-1261.
- 546
- 547 Salje, E.K.H., Taylor, R.D., Safarik, D.J., Lashley, J.C., Groat, L.A., Bismayer, U., Evans,  
548 R.J., and Friedman, R. (2012) Evidence for direct impact damage in metamict titanite  
549 CaTiSiO<sub>5</sub>. *Journal of Physics: Condensed Matter*, 24, 052202 (5 p).
- 550
- 551 Sneddon, I.N. (1965) The relation between load and penetration in the axisymmetric  
552 boussinesq problem for a punch of arbitrary profile. *International Journal of*  
553 *Engineering Science*, 3, 47-57.
- 554
- 555 Speer, J.A., and Gibbs, G.V. (1976) The crystal structure of synthetic titanite, CaTiOSiO<sub>4</sub>,  
556 and the domain texture of natural titanites. *American Mineralogist*, 61, 238–247.

557

558 Stefanovsky, S.V., Yudintsev, S.V., Nikonov, B.S., Omelianenko, B.I., and Lapina, M.I.  
559 (2000) Isomorphic capacity of synthetic sphene with respect to Gd and U. In R.W.  
560 Smith and D.W. Shoesmith, Eds., Materials Research Society Symposium  
561 Proceedings, 608, 455-460.

562

563 Taylor, M., and Brown, G.E. (1976) High-temperature structural study of the P21/a ↔ A2/a  
564 phase transition in synthetic titanite, CaTiSiO<sub>5</sub>. American Mineralogist, 61, 435–447.

565

566 Trachenko, K.O., Dove, M.T., and Salje, E.K.H. (2001) Atomistic modelling of radiation  
567 damage in zircon. Journal of Physics: Condensed Matter, 13, 1947-1959.

568

569 Vance, E.R., and Metson, J.B. (1985) Radiation damage in natural titanites. Physics and  
570 Chemistry of Minerals, 12, 255–260.

571

572 Vance, E.R., Carter, M.L., Begg, B.D., Day, R.A., and Leung, S.H.F. (2000) Solid solubilities  
573 of Pu, U, Hf, and Gd in candidate ceramic phases for actinide waste immobilization. In  
574 R.W. Smith and D.W. Shoesmith, Eds., Materials Research Society Symposium  
575 Proceedings, 608, 431-436.

576

577 Van Heurck, C., Van Tendeloo, G., Ghose, S., and Amelinckx, S. (1991) Paraelectric-  
578 antiferroelectric phase transition in titanite, CaTiSiO<sub>5</sub> II. Electron Diffraction and  
579 Electron Microscopic Studies of the Transition Dynamics. Physics and Chemistry of  
580 Minerals, 17, 604–610.

581

- 582 Weber, W.J. (2000) Models and mechanisms of irradiation-induced amorphization in  
583 ceramics. *Nuclear Instruments and Methods in Physics Research B*, 166-167, 98-106.  
584
- 585 Weber, W.J., Wald, J.W., and Matzke, H.J. (1986) Effects of self-radiation damage in Cm-  
586 doped Gd<sub>2</sub>Ti<sub>2</sub>O<sub>7</sub> and CaZrTi<sub>2</sub>O<sub>7</sub>. *Journal of Nuclear Materials*, 138, 196-209.  
587
- 588 Weber, W.J., Ewing, R.C., Catlow, C.R.A., Diaz de la Rubia, T., Hobbs, L.W., Kinoshita, C.,  
589 Matzke, H.J., Motta, A.T., Nastasi, M., Salje, E.K.H., Vance, E.R., and Zinkle S.J.  
590 (1998) Radiation effects in crystalline ceramics for the immobilization of high-level  
591 nuclear waste and plutonium. *Journal of Materials Research*, 13, 1434-1484.  
592
- 593 Zhang, M., and Salje, E.K.H. (2003) Spectroscopic characterization of metamictization and  
594 recrystallization in zircon and titanite. *Phase Transitions*, 76, 117–136.  
595
- 596 Zhang, M., Salje, E.K.H., Bismayer, U., Unruh, H.-G., Wruck, B., and Schmidt, C. (1995)  
597 Phase transition(s) in titanite CaTiSiO<sub>5</sub>: An infrared spectroscopic, dielectric response  
598 and heat capacity study. *Physics and Chemistry of Minerals*, 22, 41–49.  
599
- 600 Zhang, M., Salje, E.K.H., Malcherek, T., Bismayer, U., and Groat, L.A. (2000) Dehydration  
601 of metamict titanite: An infrared spectroscopic study. *Canadian Mineralogist*, 38, 119-  
602 130.  
603
- 604 Zhang, M., Groat, L.A., Salje, E.K.H., and Beran, A. (2001) Hydrous species in crystalline  
605 and metamict titanites. *American Mineralogist*, 86, 904–909.  
606



607 Zhang, M., Salje, E.K.H., Bismayer, U., Groat, L.A., and Malcherek, T. (2002)  
608 Metamictization and recrystallization of titanite: An infrared spectroscopic study.  
609 American Mineralogist, 87, 882–890.

610

611 Zhang, M., Salje, E.K.H., Redfern, S.A.T., Bismayer, U., and Groat, L.A. (2013) Intermediate  
612 structures in radiation damaged titanite (CaTiSiO<sub>5</sub>): a Raman spectroscopic study.  
613 Journal of Physics: Condensed Matter, 25, 115402 (12pp).

614

615 **Figure captions**

616

617 Figure 1: Evolution of the average material parameter  $P/S^2$  of virgin E2312 and after 2 h  
618 annealing at 600, 950 and 1220 K (measured after cooling to RT, respectively).

619

620 Figure 2: Evolution of average  $H(E)$  ○ and  $E$  ■ of virgin E2312 and after 2 h annealing at 600,  
621 950 and 1220 K (measured after cooling to RT, respectively).

622

623 Figure 3: Selected evolutions of  $H(E)$  ○ and  $H(O\&P)$  ☆, of virgin E2312 and after 2 h  
624 annealing at 600, 950 and 1220 K, as a function of indentation depth (measured after cooling  
625 to RT, respectively).

626

627 Figure 4: Load-displacement data of virgin E2312 and after 2 h annealing at 600, 950 and  
628 1220 K (measured after cooling to RT, respectively).

629

630 Figure 5: Comparison between the average  $H(E)$  ○ and  $H(O\&P)$  ☆ of virgin E2312 and after  
631 2 h annealing at 600, 950 and 1220 K (measured after cooling to RT, respectively).

632

633 Figure 6: Raman spectra of E2312 titanite before and after stepwise annealing at 600, 950 and  
634 1220 K (measured after cooling to RT, respectively). Peaks near  $233\text{ cm}^{-1}$  and  $423\text{ cm}^{-1}$  are  
635 marked with \*.

636

637 Figure 7: Evolution of the wavenumber and FWHM of the peak near  $233\text{ cm}^{-1}$  without and  
638 with annealing for 2h at 600, 950 and 1220 K (measured after cooling to RT, respectively).

639

640 Figure 8: Evolution of the wavenumber and FWHM of the peak near  $423\text{ cm}^{-1}$  without and  
641 with annealing for 2h at 600, 950 and 1220 K (measured after cooling to RT, respectively).

642

643 Table 1: Summary of  $P/S^2$ , elastic modulus ( $E$ ), true hardness ( $H(E)$ ), and hardness calculated  
644 after Oliver & Pharr method ( $H(O\&P)$ ) after annealing at different temperatures.

645

Annealing Temperature (K)	$P/S^2$ ( $\text{nm}^2/\text{mN}$ )	$E$ (GPa)	$H(E)$ (GPa)	$H(O\&P)$ (GPa)
295	$430.2 \pm 6.2$	$161.2 \pm 1.9$	$12.4 \pm 0.2$	$11.5 \pm 0.3$
600	$422.9 \pm 4.9$	$157.4 \pm 1.5$	$11.7 \pm 0.1$	$10.9 \pm 0.2$
950	$342.5 \pm 7.6$	$163.2 \pm 3$	$10.1 \pm 0.2$	$9.5 \pm 0.4$
1220	$348.8 \pm 10.3$	$171.3 \pm 2.5$	$11.2 \pm 0.3$	$10.2 \pm 0.5$

646

647

648 Table 2: Summary of band positions and FWHMs of selected Raman peaks after annealing at  
649 different temperatures.

650

Annealing Temperature (K)	Band Position ( $\text{cm}^{-1}$ )	FWHM ( $\text{cm}^{-1}$ )	Band Position ( $\text{cm}^{-1}$ )	FWHM ( $\text{cm}^{-1}$ )
295	$232.6 \pm 0.4$	$20.7 \pm 3.2$	$423 \pm 0.4$	$37 \pm 3.9$
600	$232.6 \pm 0.5$	$21.6 \pm 3.3$	$423.5 \pm 0.4$	$37.2 \pm 3.8$
950	$236.8 \pm 0.3$	$12.1 \pm 1.8$	$426.7 \pm 0.4$	$32 \pm 2.5$
1220	$237.4 \pm 0.3$	$9.6 \pm 1.6$	$427.5 \pm 0.4$	$28.3 \pm 2.9$

651

Figure 1

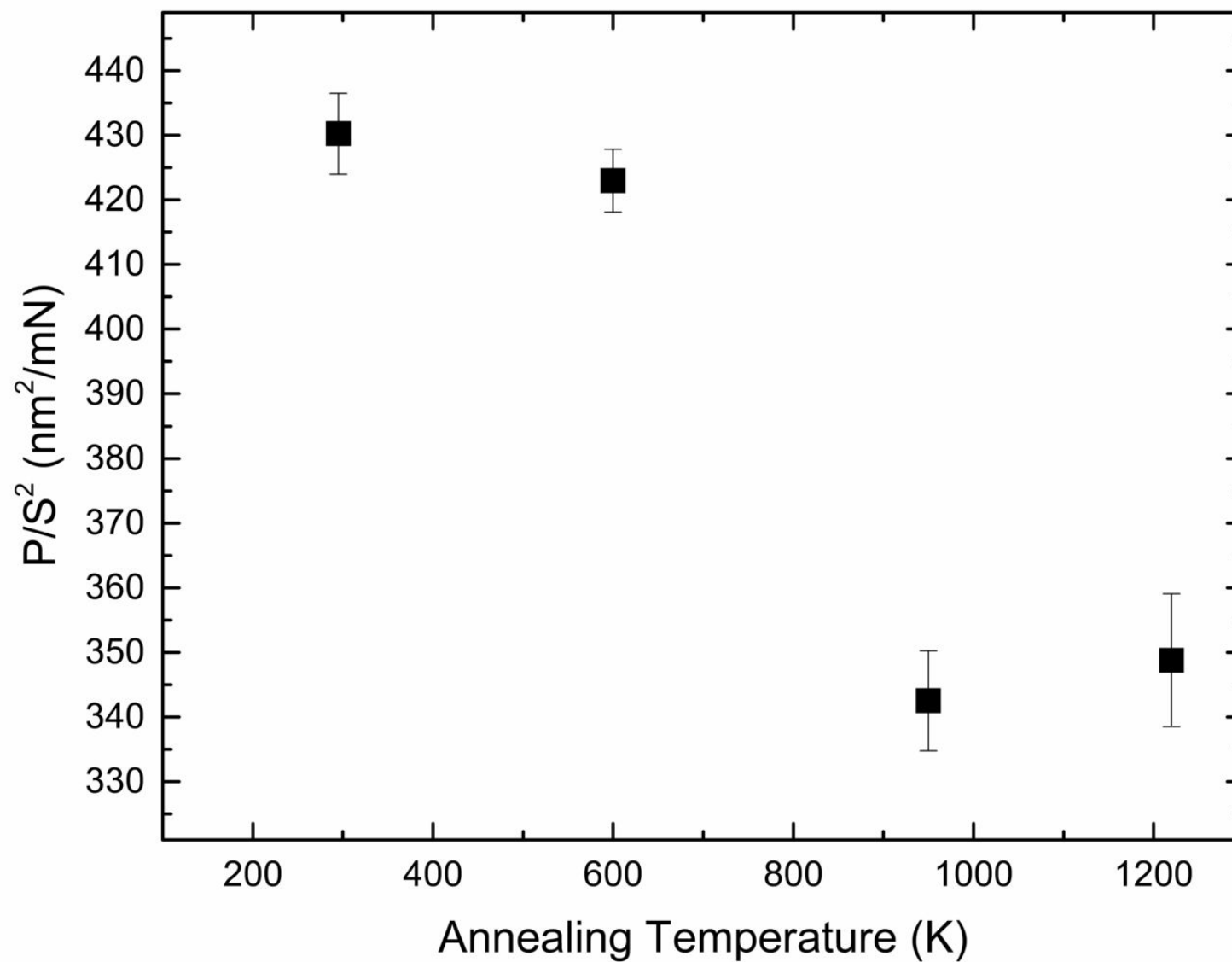


Figure 2

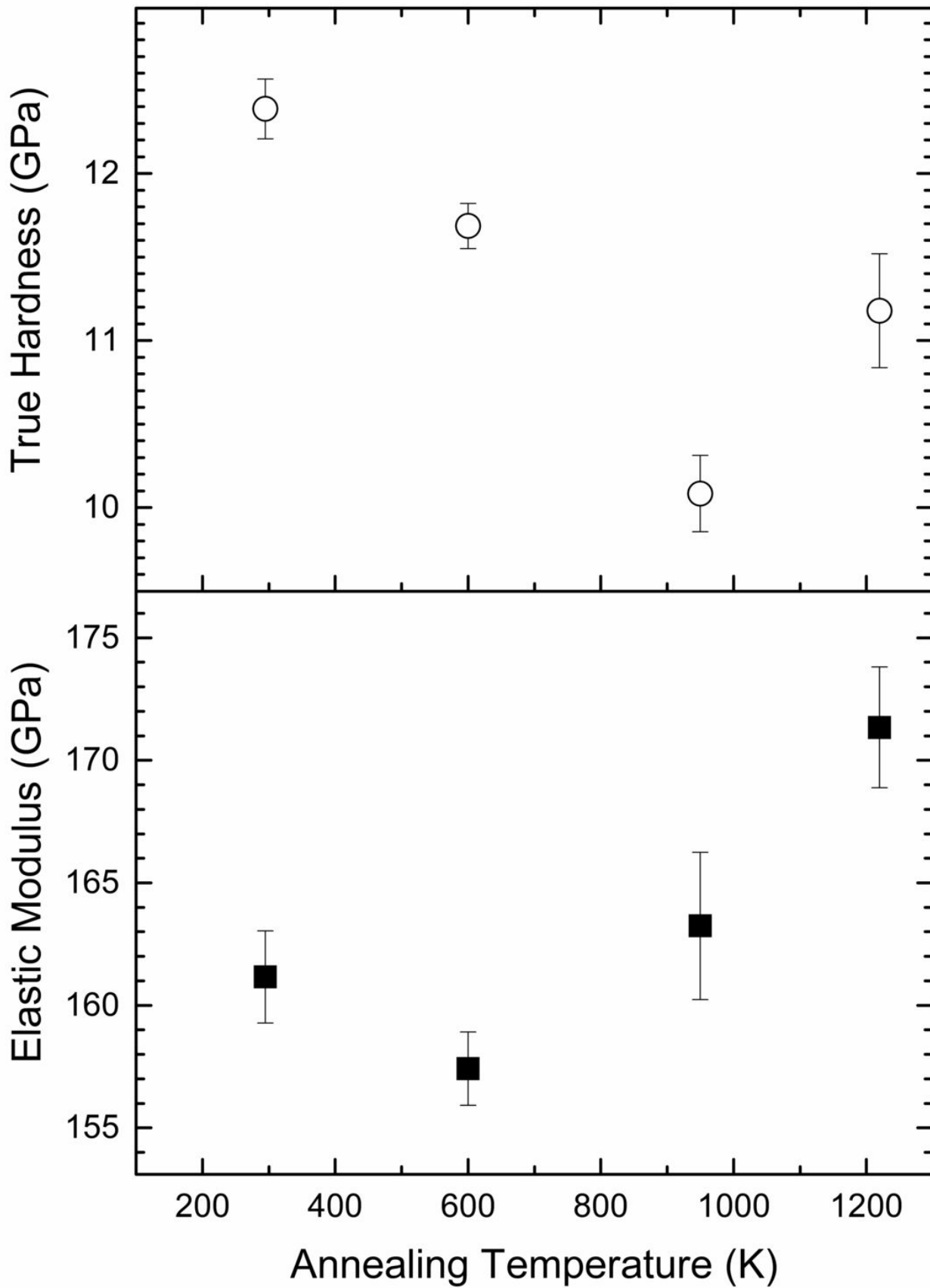
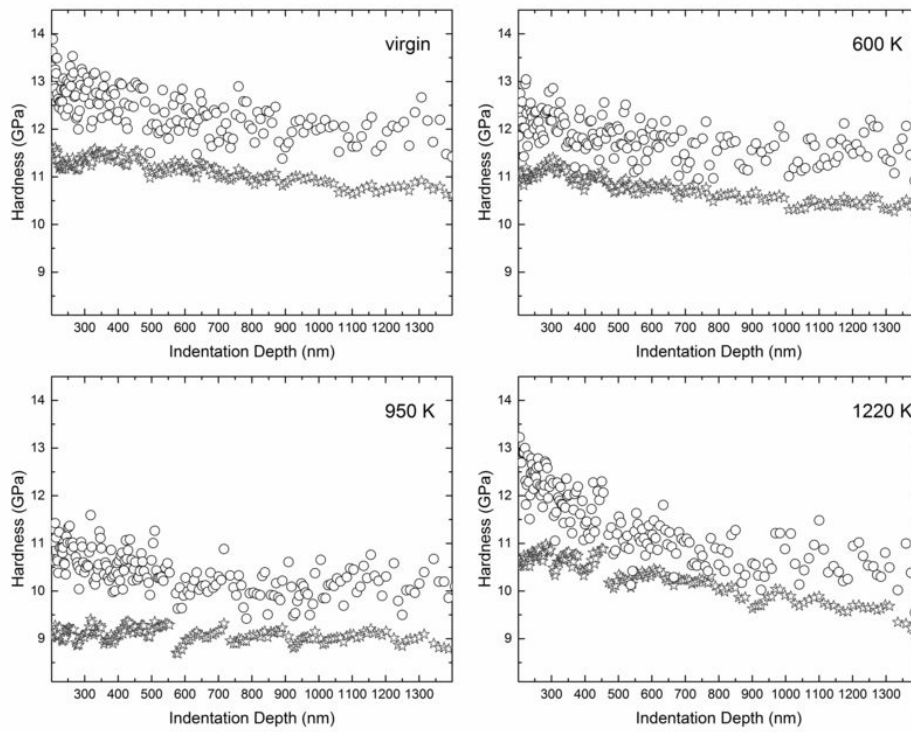


Figure 3



# Figure 4

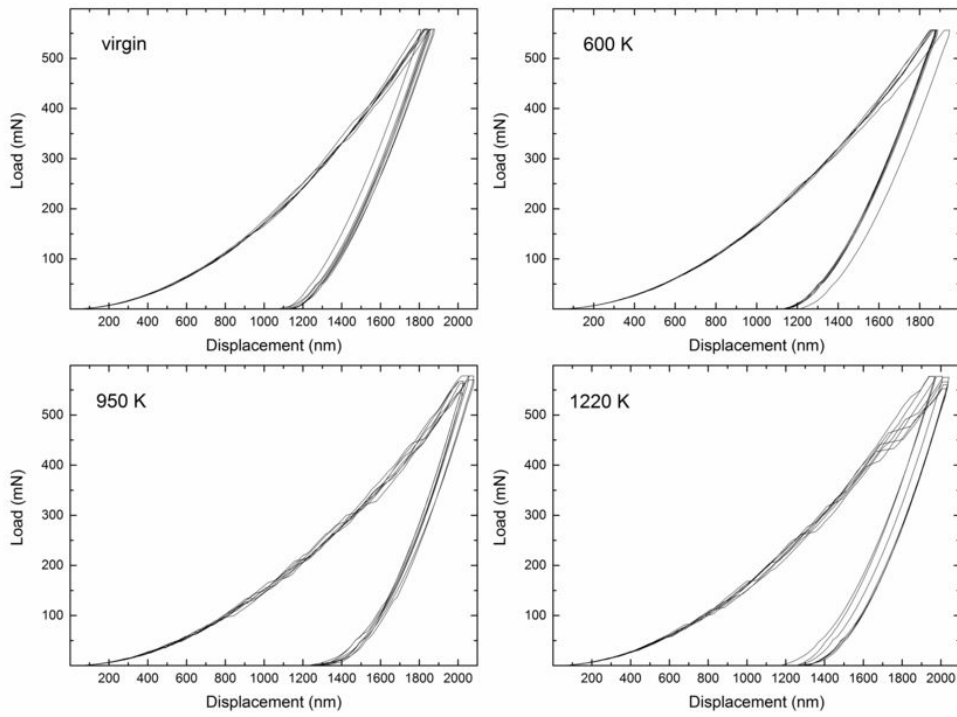


Figure 5

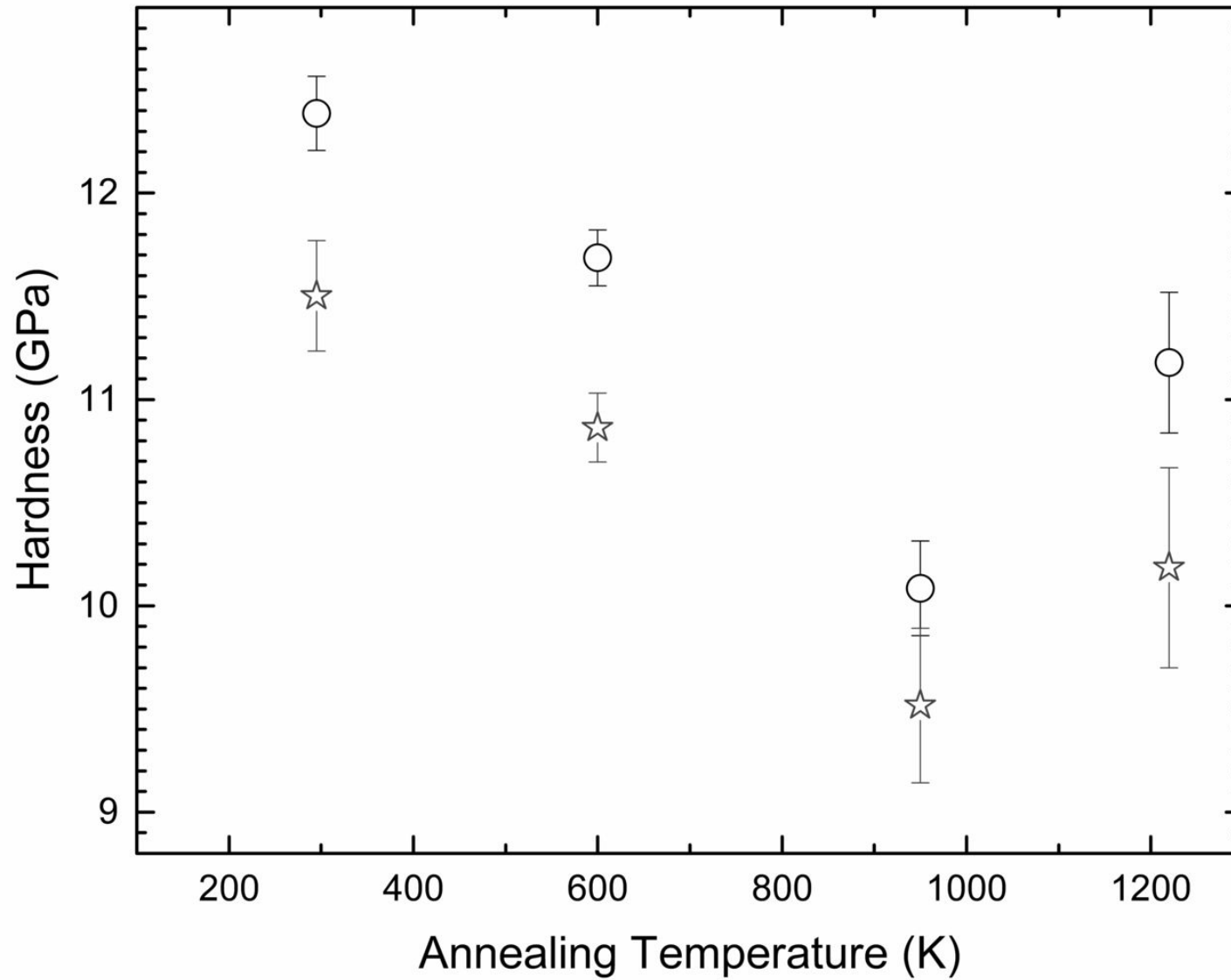


Figure 6

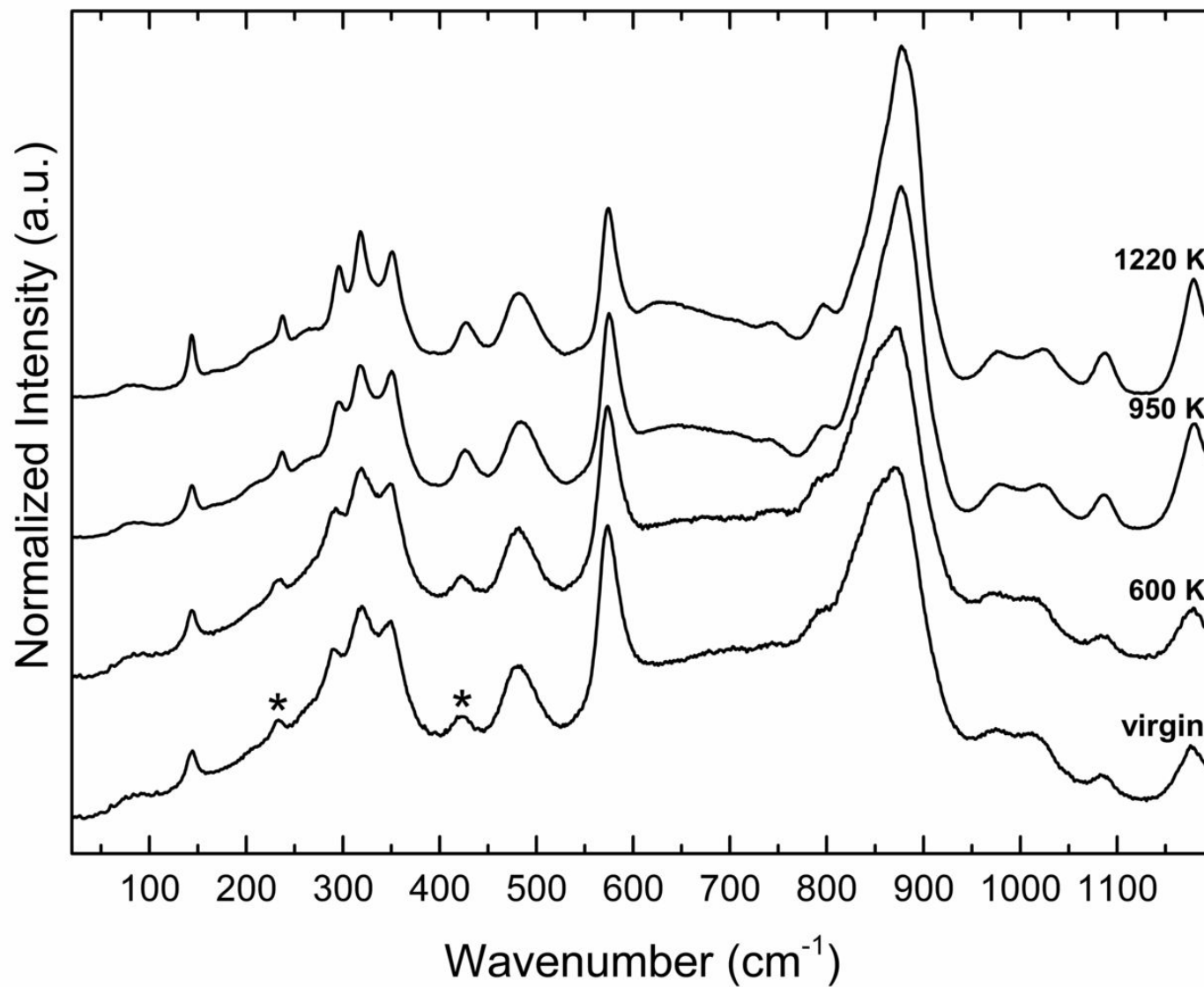




Figure 7

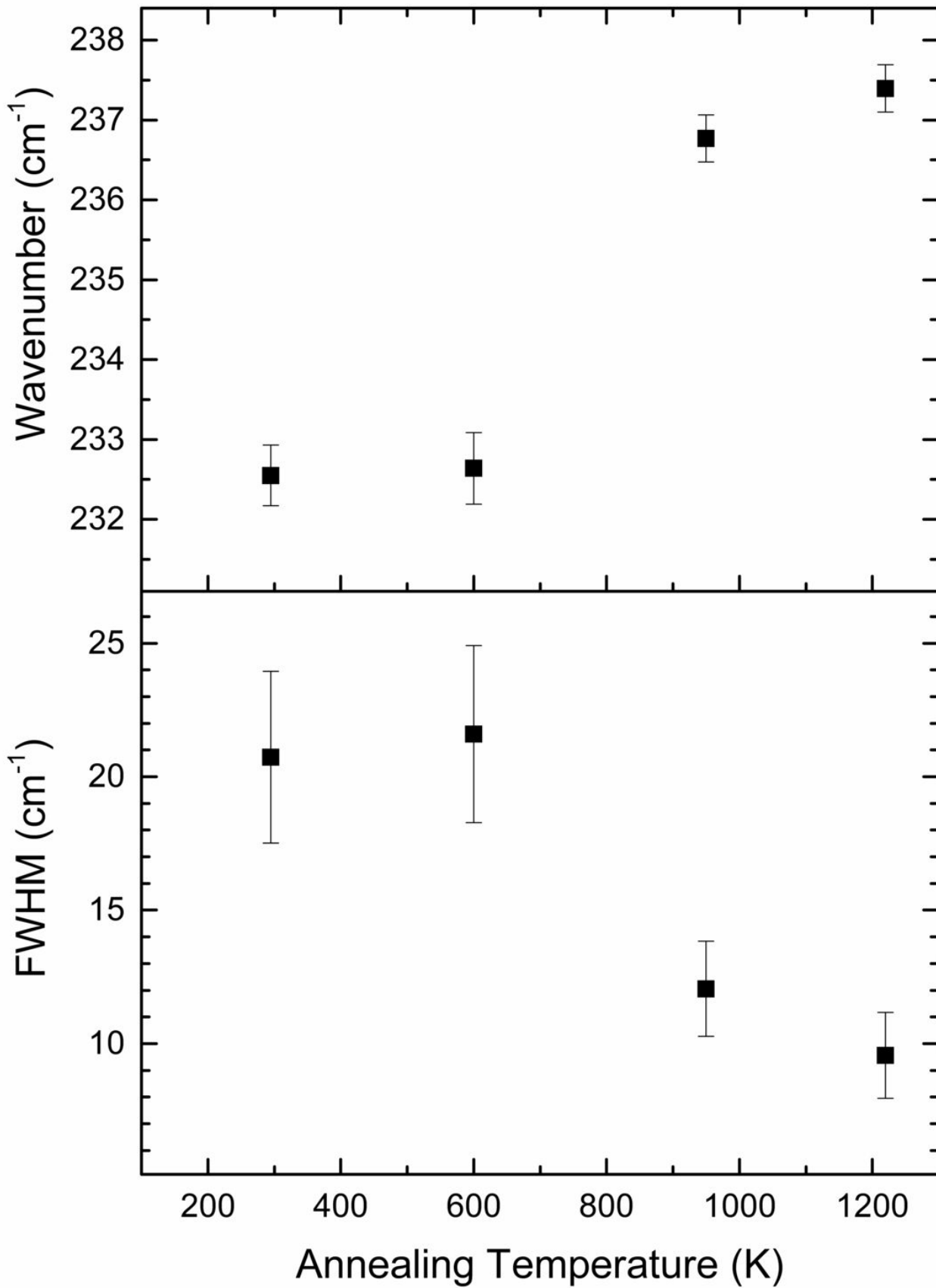
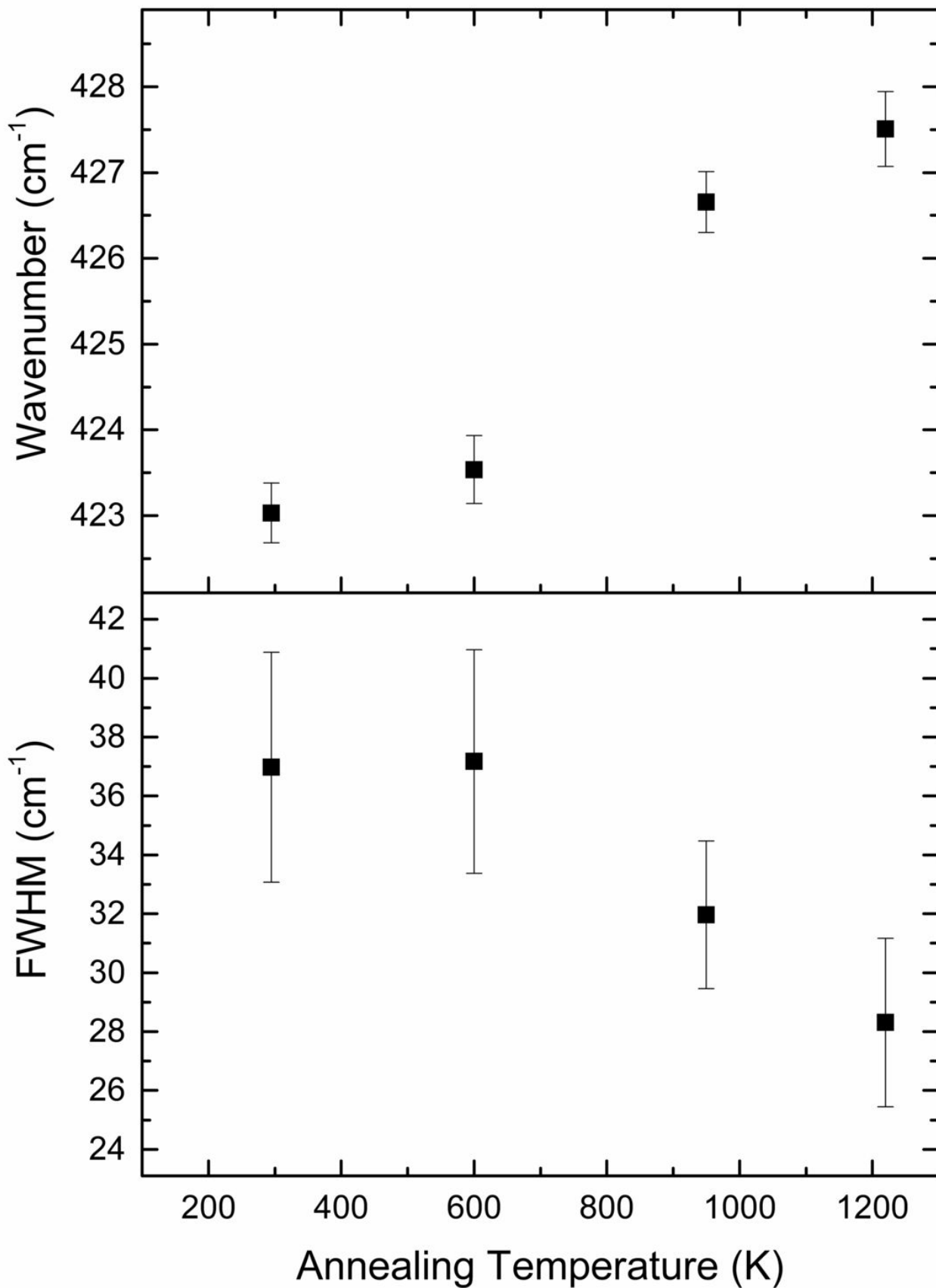


Figure 8



<b>Annealing Temperature (K)</b>	<b><math>P/S^2</math> (nm<sup>2</sup>/mN)</b>	<b><math>E</math> (GPa)</b>	<b><math>H(E)</math> (GPa)</b>	<b><math>H(O\&amp;P)</math> (GPa)</b>
295	430.2 ± 6.2	161.2 ± 1.9	12.4 ± 0.2	11.5 ± 0.3
600	422.9 ± 4.9	157.4 ± 1.5	11.7 ± 0.1	10.9 ± 0.2
950	342.5 ± 7.6	163.2 ± 3	10.1 ± 0.2	9.5 ± 0.4
1220	348.8 ± 10.3	171.3 ± 2.5	11.2 ± 0.3	10.2 ± 0.5

<b>Annealing Temperature (K)</b>	<b>Band Position (cm<sup>-1</sup>)</b>	<b>FWHM (cm<sup>-1</sup>)</b>	<b>Band Position (cm<sup>-1</sup>)</b>	<b>FWHM (cm<sup>-1</sup>)</b>
295	232.6 ± 0.4	20.7 ± 3.2	423 ± 0.4	37 ± 3.9
600	232.6 ± 0.5	21.6 ± 3.3	423.5 ± 0.4	37.2 ± 3.8
950	236.8 ± 0.3	12.1 ± 1.8	426.7 ± 0.4	32 ± 2.5
1220	237.4 ± 0.3	9.6 ± 1.6	427.5 ± 0.4	28.3 ± 2.9